optica

Observation of spin-polarized directive coupling of light at bound states in the continuum: supplementary material

GIANLUIGI ZITO*[1,*], SILVIA ROMANO[2], STEFANO CABRINI[3], GIUSEPPE CALAFIORE[3], ANNA CHIARA DE LUCA[1], ERIKA PENZO[3], AND VITO MOCELLA[2,*]

[1] National Research Council, Institute of Protein Biochemistry, Via Pietro Castellino, Naples, 80131, Italy
[2] National Research Council, Institute of Microlectronics and Microsystems, Via Pietro Castellino, Naples, 80131, Italy
[3] National Research Laboratory of Berkeley, Molecular Foundry, Berkeley, CA 94720, USA
* Corresponding author: g.zito@ibp.cnr.it, vito.mocella@imm.na.cnr.it

Published 30 September 2019

This document provides supplementary information to "Observation of spin-polarized directive coupling of light at bound states in the continuum," https://doi.org/10.1364/OPTICA.6.001305. Section 1 includes methods and details for numerical simulations. Section 2 provides additional text about the physical interpretation of the phenomenon and specific cases not reported in the main paper (quasi-bound state in the continuum and non-symmetry protected degenerate modes). Section 3 provides details of fabrication and optical characterization. In Section 4, a theoretical model is presented.

1. NUMERICAL SIMULATIONS

Numerical simulation of the excited modes in the structure were carried out by using a full three-dimensional rigorous coupled wave approach (RCWA) based on a Fourier modal expansion. Additional finite difference time domain (FDTD) simulations, using commercial software FULLWAVE (https://optics.synopsys.com/rsoft/rsoft-passive-device-fullwave.html) allowed us eliciting the spin-dependent character of the the excited states. The computational domain was limited to a unit cell of the PhCM. We applied Bloch periodic boundary condition to surfaces along x-, y-directions. On top and bottom surfaces, normal to the z-direction, and far enough from the membrane, we imposed perfectly-matched-layer absorbing boundary conditions [1, 2]. The adapted mesh along z had a size-step of 3 nm inside the PhCM and increased outside, up to a value of 20 nm. The time step was chosen to be well below the stability limit. Steady-state regime was reached after 10^5 optical cycles. As a further check, finite element method-based simulations, carried out with Comsol Multiphysics 5.2a, were finally used to verify the consistence of all simulations and the properties of the symmetry-protected BIC modes. A BIC mode point is numerically calculated as an asymptotic mode, with progressively higher Q-factor but only asymptotically diverging even if very large (truncation at $Q = 10^9$ in our simulations). The calculation time determines the spectral resolution and hence the numerical Q-factor, without changing the feature of the mode for what concerns symmetries etc. Once determined the approximated frequency of the mode, any far field source, regardless of its polarization, can be used at a frequency close to the ideal one to excite the response of the system. Once determined the electromagnetic field $(\boldsymbol{E}, \boldsymbol{H})$ of the modes, we calculated the linear momentum density $\boldsymbol{\Pi}$ and SAM density $\boldsymbol{S}$ according to Ref. [3, 4], as described in the main text. The amplification of the field is limited only by the numerical precision of the simulation, reaching values as large as $10^8 E_i$, with E_i input field amplitude.

2. FIELD STRUCTURE OF THE BIC MODE AND SPIN-MOMENTUM BOUNDARY CONDITIONS

Considering an infinite PhC slab with a square lattice in the xy plane, either for a BIC field with TM-like structure of main components (H_x, H_y, E_z) or TE-like components (E_x, E_y, H_z), each amplitude obeys Floquet-Bloch theorem with the further condition of total uncoupling from the continuum, thus the field must be evanescent out of the slab. In a real structure a partial coupling is always possible and the continuum field amplitude u_0 must be included in the equation. Let us indicate the generic planar component of the magnetic field as H. Experimentally, we observe four waves excited at the BIC propagating in the xy plane and that can be associated to the basic four $\boldsymbol{\Gamma}^{(2)}$ waves of the reciprocal lattice [5], whereas higher order Bloch's waves have negligible contribution. Thus, neglecting other contributions, we can write the field of the *quasi*-BIC mode as

$$\begin{aligned}H(\boldsymbol{r}) &= u_0(\boldsymbol{r}) + u(\boldsymbol{r})\\ &= u_0 e^{i\boldsymbol{k}_i\cdot\boldsymbol{r}} + u(x,y)u(z)\\ &= u_0 e^{i\boldsymbol{k}_i\cdot\boldsymbol{r}} + f_P(x,y)\sum_{j=1}^{4} b_j(z)e^{i\boldsymbol{\Gamma}_j^{(2)}\cdot\boldsymbol{r}},\end{aligned} \tag{S1}$$

where

$$\boldsymbol{\Gamma}_j^{(2)} = \begin{cases} \boldsymbol{k}_R = (\beta_0, 0, 0), & j=1,\\ \boldsymbol{k}_B = (0, -\beta_0, 0), & j=2,\\ \boldsymbol{k}_L = (-\beta_0, 0, 0), & j=3,\\ \boldsymbol{k}_T = (0, \beta_0, 0), & j=4,\end{cases}$$

and of course $\boldsymbol{r} = (x, y, z)$, with $\beta_0 = 2\pi/a$. In the above expression, the periodicity along the slab symmetry axes is ensured by the harmonic functions of the $\boldsymbol{\Gamma}^{(2)}$ wave vectors, and by the periodic function $f_P(x,y)$ introduced as an envelope to account for a more general functional behavior of the field component in the unit cell. Provided that for $0 < z < h$ the actual expression for each $b_j(z)$ depends on the system, we can explicitly write the evanescent decay behavior out of the slab for the j-th Bloch component as

$$b_j(z) = \begin{cases} b_h e^{-\kappa_1(z-h)} & \text{for } z \geq h,\\ b_0 e^{-\kappa_2 z} & \text{for } z \leq 0,\end{cases} \tag{S2}$$

where $|\kappa_1| > |\kappa_2|$ are the two imaginary parts of the complex wave vectors of the field at the interfaces $z = h$ (Si_3N_4/air) and $z = 0$ (Si_3N_4/SiO_2) (Fig. S1).

A crucial point is that the imaginary components of the complex wave vector have opposite directions along the z-axis so that in our reference system while $\kappa_1 > 0$, on the other hand $\kappa_2 < 0$, which is consistent with the attenuation of the wave for $z < 0$. The only presence of an inhomogeneous structure of the field along the z-axis, provided by the evanescent decay, ensures the existence of a *non-null* component of SAM, say $\boldsymbol{s}$, that is orthogonal to the phase component of the wave vectors (real part) $\boldsymbol{k}_{1,2}$, where the index is respectively associated to the regions 1 and 2. According to recent papers [6, 7], as here depicted in Fig. S1, thus the possible triads formed by $\{\boldsymbol{k}_{1,2}, \boldsymbol{\kappa}_{1,2}, \boldsymbol{s}_{1,2}\}$ must be locked in such a way that

$$\text{sign}(\boldsymbol{s}) = \begin{cases} \text{sign}(\boldsymbol{k}) & \text{for } \boldsymbol{\kappa} > 0\\ -\text{sign}(\boldsymbol{k}) & \text{for } \boldsymbol{\kappa} < 0.\end{cases} \tag{S3}$$

Since the sign of $\boldsymbol{\kappa}$ is fixed by the specific interface (region 1 or 2), the above locking equation reduces the possible solutions of the system that can be excited by an optical stimulus to four surface waves - two for each interface of the system- that will propagate along a given direction. The specific axis of propagation of the excited solution depends on the system geometry, its symmetries and the phase-matching condition with the input momentum. In particular, we have indicated the x-axis in Fig. S1. In more detail, the admitted solutions are, at a *fixed interface* (say $z = h$, region 2 for instance), two *counter-propagating* surface waves with *opposite transverse SAM* (Fig. S1). It also true that two *counter-propagating* surface waves, at the *two separate interfaces,* $z = 0$ *and* $z = h$, will have *the same sign of transverse SAM*. This last can also be read as "two *co-propagating* surface waves at *opposite* interfaces will have *opposite* transverse SAM".

Such a mechanism of spin-momentum locking can be used to manipulate radiation coupling towards preferential directions. Indeed, an input excitation with a definite spin stimulates the optical solution of the

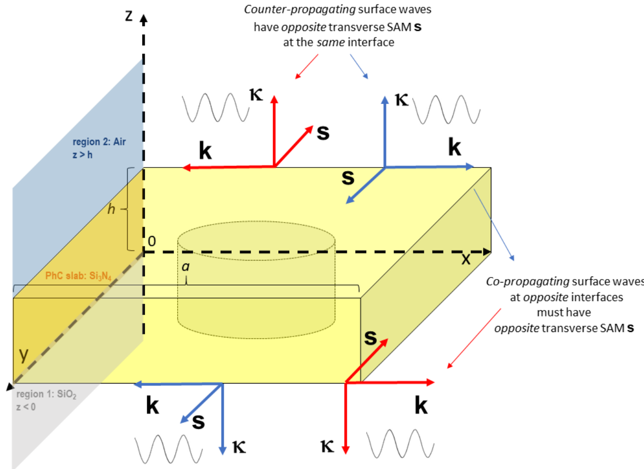

Fig. S1. Spin-momentum locking scheme. (a) The evanescent decay direction in the positive and negative z half spaces locks the relative transverse spin and phase-propagation orientation according to eq. (S3).

system having same spin, condition of *spin-matching* that is discussed in more detail below. When the spin stimulated by the external field is transverse to the direction of propagation of the generated wave, its phase propagation direction is locked to the spin. This mechanism therefore will select the surface waves at the interfaces of the system according to the scheme reported in Fig. S1. Such an effect is also called *spin-polarized directive coupling* and the photonic system capable of this property shows a *chiral behavior*, *i.e.* a response to the external field that is dependent on the input circular polarization. We can say without loss of generality that such a mechanism obeys *dynamic boundary conditions*, *i.e.* not only related to the geometry of the system and its admitted field solutions, but related also to the dynamics of the field and its evolution in time since the momentum is locked to the spin.

The scheme reported in Fig. S1 for waves propagating along the x-axis is actually not only limited to this direction. As mentioned above, we experimentally observe 4 waves along the four-fold symmetry axes of the PhC slab. Back to the field structure in eq. (S1), we can see that the Bloch's waves are two counter-propagating waves along the x-axis and other two counter-propagating waves along the y-axis, reflecting indeed the rotational symmetry of the system. This means that while for a homogeneous medium any direction of propagation in the plane of the interface could be excited under the proper phase-matching condition with the input wave, in case of the PhC slab only the guided waves that agree with the dispersion relations of the photonic structure can be excited. In our case, at normal incidence, this leads to the the four $\boldsymbol{\Gamma}^{(2)}$ waves propagating in the plane of the structure.

It is worth stressing again that no waves were observed (at least of intensity large enough to be detected) for a frequency detuned from the BIC resonance. As discussed in the main paper, we argue that the BIC resonant mechanism amplifies the local field and, as a consequence, it also amplifies its actual Bloch's wave components, and this is why the $\boldsymbol{\Gamma}^{(2)}$ directions of propagation emerge from the system.

Let us now give more insight into the spin-dependent propagation that is finally responsible of the chiral behavior experimentally observed when illuminating our photonic structure with a collimated spin-polarized beam. Indeed, the external optical stimulus of a definite spin will excite preferentially the concordant spin, but spin-momentum locking breaks the two-fold degeneracy of the mirror-symmetric system (geometrically speaking) producing only *one* acceptable surface

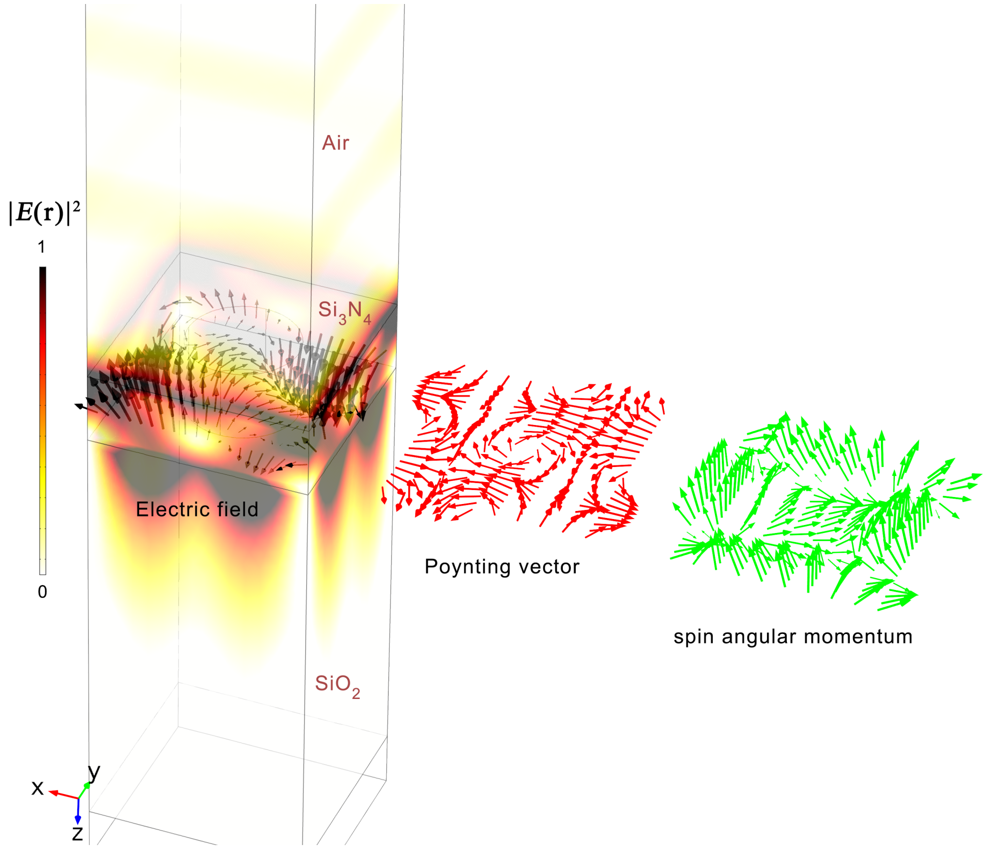

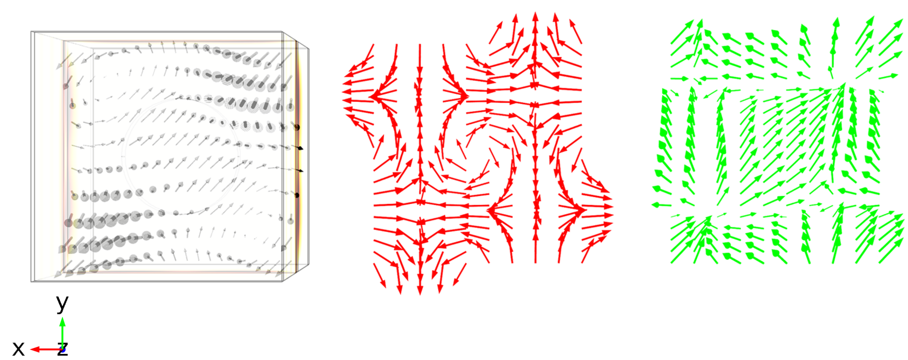

Fig. S2. Mode profile of a symmetry-protected TM *quasi*-BIC for h = 120 nm: $|\boldsymbol{E}|^2$-map inside the unit cell of the square lattice together with the vector map of $\boldsymbol{E}$ at $z = h/2$ of the PhCM. The electric field is structured in an optical skyrmion lattice and shows cycloidal rotation in the the (x, z)-planes. The Poynting vector map clearly shows that light is confined in the (x, y)-plane of the crystal. The SAM density map shows a pronounced component that is transverse to the the (x, y)-plane and transverse to the direction of propagation.

wave on *each* interface instead of two, and being the waves on opposite interfaces characterized by opposite directions of propagation. A second crucial point is that the amplitude of the field at the two different interfaces depends on the interface in that simply $b_h \neq b_0$ (see eq. S2). Thus, the intensity of the out-coupled field along a given direction will be dependent on the *spin-matching*, and will be no more mirror-symmetric for a given input polarization. Despite the original geometric symmetry of the system, the spin-momentum locking provides a dynamic boundary condition that breaks the pure geometric degeneracy inducing a chiral behavior because $b_h \neq b_0$.

We can now move a step forward considering the finite size of the slab. We have talked of surface waves on apparently distant interfaces, but we must now consider the actual case of a distance h even inferior than the same optical wavelength λ. In this scenario, the transverse spin and relative momentum locking is not only relevant at the interface, but becomes dominant also inside the slab as shown in Fig. 2e-f. The numerical simulations in Fig. 2, Fig. S2-S3 reveal indeed such a circumstance. We can say that the tight confinement of the field with amplified local field, and a continuous variation across the interfaces that imposes large transverse spin also inside the slab, leads to a macroscopic spin-polarized directive coupling. Furthermore, the continuity of field across the slab section results in a vortex structure.

Spin-matching condition. For what specifically concerns the spin-matching condition, we must consider that the electric optical response of any system is provided by the induced dipole moment in the homogeneous polarizable material, which is simply proportional, for an isotropic medium with diagonal dielectric tensor $\epsilon_x = \epsilon_y = \epsilon_z$, to the input field $\boldsymbol{E_i}(\boldsymbol{r})$. The input field is a complex vector that in case of well-defined ellipse of polarization will have components with a coherent phase relation, from which of course its circular polarization, or elliptical in general, will result. The induced dipole moment in a homogeneous polarizable small particle will therefore inherit the spin of the input, radiating a field with same spin along the forward scattering direction (and opposite spin in the back-scattering direction because of time reversal symmetry). Another effort must be made to clarify the spin-matching condition between the SAM of the collimated Gaussian laser beam (or plane wave in approximation) used as input field and the SAM structure of the excitable solution in our photonic structure. Indeed, the optical field solution is now given by the collective response of all phase-retarded dipole moments in each unit cell. The solution field structure will depend on the dielectric function and geometry of the system. A numerical representation is provided in Fig. 2 and in Figs. S2-S3 (say TM-like modes) depending on the slab thickness h. Either in case of TE-like or TM-like structure (actually hybrid), the transverse SAM density has in general a three-dimensional distribution, being the vector not confined in a specific plane or direction, as clearly visible in Fig. 2, S2-S3, and therefore a good matching with the out-of-plane longitudinal spin of an ideally free-space wave is possible. In particular, as shown in Fig. 2e-f, in the xz cut plane where the energy density of the mode is maximum, the transverse SAM has major component just along the input spin direction. Furthermore, in consistency with the spin-momentum locking boundary conditions, the sign of the transverse component in the evanescent regions flips from one interface to the other in agreement with eq. S3. Since the field intensity is asymmetric along z, thus the amount of input light coupled towards a specific direction results spin-polarization dependent.

As clearly visible in Fig. 2c-d, a vortex of topological charge $|q| = 1$ emerges in the Poynting vector structure of each unit cell. Importantly, the sign of the topological charge is dictated by the specific input SAM. Indeed, since the input spin determines the transverse SAM at the boundary, and hence the associated field structure, the sign of q is dependent on the transverse SAM structure (Fig. S2-S3).

We propose a model in Sec. 4 to describe qualitatively the experimental results reported in Fig. 4 and Fig. 5, which basically takes into account the Berry phase introduced by the optical transformation that any input polarized beam undergoes because of beam redirection upon scattering (along well defined directions in the PhCM plane at the BIC). Opposite directions of propagation, say positive and negative $\hat{\boldsymbol{x}}$, are characterized by a different Berry phase, which in turn affect the results also in case of linear input polarization. While the theory is based on a single particle scattering, the BIC radiation in the plane may be seen as coupled dipole sources or nanoantennas with a square lattice arrangement, which gives the narrow wave vectors dispersion of the scattered radiation along the symmetry axes of the crystal.

3. SAMPLE FABRICATION AND CHARACTERIZATION

The PhCM samples were 1 ×1 mm^2 large and consisted of air-cylindrical holes in a square lattice. The patterned area was realized on a Si_3N_4 layer deposited on a quartz slide by means of plasma-enhanced chemical vapor deposition (PECVD). The square lattice was defined on ZEP 520, a positive electron beam resist, by using a high-precision nanofabrication process based on high-voltage electron beam lithography (Vistec VB300UHR EWF). The resist mask was then transferred by reactive ion etching (RIE) in an Oxford Instruments PlasmaLab 80 Plus tool, using CHF_3 and O_2, at room temperature. Figure 1b shows the final result. The lattice parameters were optimized in order to have the resonant behavior of the structure around 530-540 nm for the sample in the visible range and 1550 nm for the sample in the infrared range. The lattice hole radius was $r = a/4$, whereas the thickness of the PhCM was in the range $h = (0.1\lambda, 0.35\lambda)$, with λ given by the free-space wavelength of the expected BIC. Such values were determined according to the procedure described in Ref. [8]. In particular, experimentally by AFM microscopy we measured for the various samples, $h = 54, 85, 120, 144, 175$ nm.

The samples were investigated by means of a supercontinuum laser (SuperK Extreme NKT Photonics), which allows a high output power, a broad spectrum, and a high degree of spatial coherence. The emission spectrum was 400 - 2400 nm. By using acousto-optic tunable filters, we converted it into an ultra-tunable laser with up to 8 simultaneous laser lines. The sample was mounted on a motorized rotation stage, allowing rotational steps of 0.01°. The transmitted spectrum was collected by a spectrometer (HR4000, Ocean Optics) with a resolution of 0.25 nm and a range of 350 - 800 nm. The collimated beam incident on the sample had a beam waist of ∼ 0.5 mm. The radiation outcoupled from the sides of the sample was analyzed to determine the Stokes parameters of each beam.

In an ideal PhCM, the quality factor of a BIC peak tends to infinity. However, in real devices, the resonance width is limited by finite sample size, effective collimation and scattering losses due to the sample imperfections [9]. As such, the total Q-factor of the resonator can be written as $1/Q = 1/Q_V + 1/Q_H + 1/Q_A$, in which the term Q_V depends on the coupling efficiency to incident light and corresponds to the intrinsic BIC quality factor; Q_H measures the horizontal in-plane losses due to the finite lateral extension of the pattern; and Q_A accounts for the material absorption and scattering losses. The measured Q-factor is consistent with a near-BIC regime, as corresponding to a linewidth $\simeq 0.5$ nm (Fig. 3b) due to finite lateral confinement as in previous reports [9, 10].

4. MODEL BASED ON GEOMETRIC PARALLEL TRANSPORT OF POLARIZATION

The coherent scattering process of a photon propagating along $\hat{\boldsymbol{z}}$ and redirected along $\pm\hat{\boldsymbol{x}}$ and $\pm\hat{\boldsymbol{y}}$ in the plane of the PhC can be described using the theory of geometric parallel transport of light polarization. We follow the framework described in [3, 11, 12], which we explicitly refer to. In particular, in the following we will review this formalism before adapting it to our case. Let us consider a paraxial optical field of polarization $\boldsymbol{E_i}(\boldsymbol{r}) \equiv (E^+, E^-, 0)^T$, *i.e.* of circular components E^+ and E^- and null longitudinal z-component in the global circular representation of polarization. Circular basis vectors are related to the Cartesian linear representation through $\boldsymbol{u}_\pm = \frac{1}{\sqrt{2}}(\boldsymbol{u_x} \pm i\boldsymbol{u_y})$, whereas the components can be transformed according to $E^\pm = \frac{1}{\sqrt{2}}(E_x \mp iE_y)$. Given respectively α and β the orientation angles of the HWP and QWP fast axes with respect to the input $\boldsymbol{u_x}$-polarizer (Fig. 3a, main paper), their Jones matrices $\hat{H}(\alpha)$ and $\hat{Q}(\beta)$ are expressed in the linear representation, for an ideal paraxial field with null z-component, according to

$$\hat{H}(\alpha) = \begin{pmatrix} \cos(2\alpha) & \sin(2\alpha) & 0 \\ \sin(2\alpha) & -\cos(2\alpha) & 0 \\ 0 & 0 & 0 \end{pmatrix}, \tag{S4}$$

$$\hat{Q}(\beta) = \begin{pmatrix} \cos^2(\beta) + i\sin^2(\beta) & (1-i)\sin(\beta)\cos(\beta) & 0 \\ (1-i)\sin(\beta)\cos(\beta) & i\cos^2(\beta) + \sin^2(\beta) & 0 \\ 0 & 0 & 0 \end{pmatrix}. \tag{S5}$$

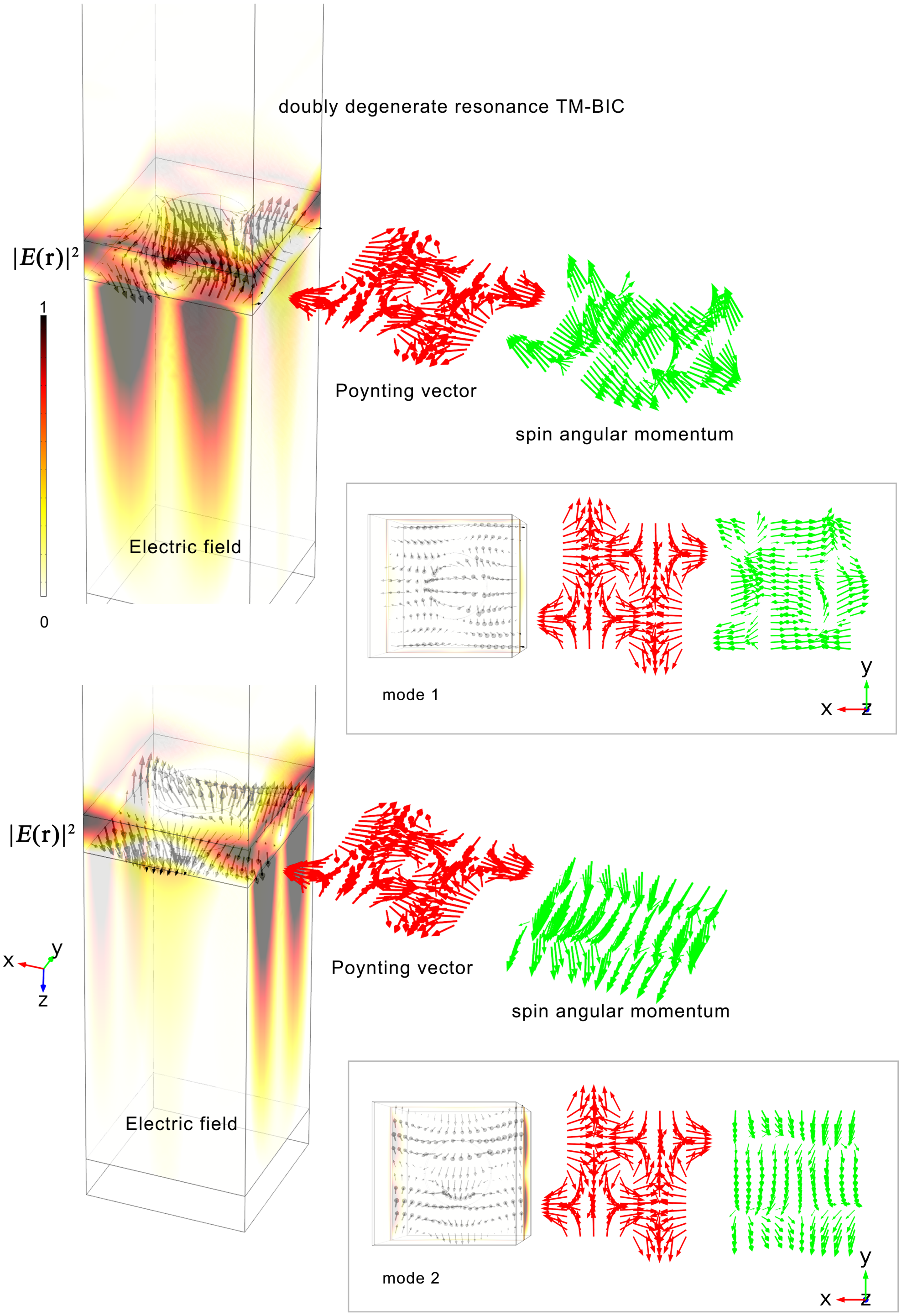

Fig. S3. Mode profile of a resonance-trapped TM BIC for h = 90 nm: $|\boldsymbol{E}|^2$-map inside the unit cell of the square lattice together with the vector map of $\boldsymbol{E}$ at $z = h/2$ of the PhCM for the doubly-degenerate profile (modes 1 and 2). The Poynting vector map clearly shows that light is confined in the (x, y)-plane of the crystal. The SAM density map shows a pronounced component that is transverse to the the (x, y)-plane and transverse to the direction of propagation.

Therefore, the input paraxial field on the PhCM can be written as

$$\boldsymbol{E_i}(\alpha, \beta) = \hat{V}_c \hat{Q}(\beta) \hat{H}(\alpha) E_x \boldsymbol{u_x}, \tag{S6}$$

being $E_x \boldsymbol{u_x}$ the input laser state and $\hat{V}_c$ the Cartesian-to-circular representation transform

$$\hat{V}_c = \frac{1}{\sqrt{2}} \begin{pmatrix} 1 & i & 0 \\ 1 & -i & 0 \\ 0 & 0 & \sqrt{2} \end{pmatrix}. \tag{S7}$$

Non-paraxial redirection of input plane waves having $\boldsymbol{k_i} = \frac{2\pi}{\lambda}\hat{\boldsymbol{z}}$ can be described, in the adiabatic approximation, by considering that input polarization is not changed in the local frame attached to the redirected wavevectors $\boldsymbol{k}$ [11]. The output polarization $\tilde{\boldsymbol{E}}_{\boldsymbol{o}}(\boldsymbol{k})$ of a partial wave redirected in the momentum space in the direction (θ_r, ϕ), *i.e.* having components $k_x = k\sin\theta_r\cos\phi, k_y = k\sin\theta_r\sin\phi, k_z = k\cos\theta_r$, with $k = 2\pi/a$, can be written

$$\tilde{\boldsymbol{E}}_{\boldsymbol{o}}(\theta_r, \phi) \propto \hat{\mathcal{U}}(\theta_r, \phi)\boldsymbol{E_i}. \tag{S8}$$

The angles (θ_r, ϕ) serve both as real-space coordinates for the incident field $\boldsymbol{E_i}$ (for which $\theta_r = \theta_i = 0$) and momentum-space coordinates for the refracted field $\tilde{\boldsymbol{E}}_{\boldsymbol{o}}$. The nondiagonal unitary transformation $\hat{\mathcal{U}}(\theta_r, \phi)$ is defined in the global circular basis as

$$\hat{\mathcal{U}}(\theta_r, \phi) = \begin{pmatrix} a & -be^{-2i\phi} & \sqrt{2ab}e^{-i\phi} \\ -be^{2i\phi} & a & \sqrt{2ab}e^{i\phi} \\ -\sqrt{2ab}e^{i\phi} & -\sqrt{2ab}e^{-i\phi} & a-b \end{pmatrix}, \tag{S9}$$

with $a = \cos^2\theta_r/2$ and $b = \sin^2\theta_r/2$, and it is characterized by off-diagonal geometric-phase elements (ϕ-dependence) from which spin-to-orbital angular momentum conversion (SOC) stems. The angle θ_r belongs to the range $(0, \theta_c)$, where in the limiting case $\theta_c = \pi/2$, whereas $\phi \in (0, 2\pi)$. Any input circularly polarized vortex of helicity state σ and orbital angular momentum l (which can be also zero) will be transformed in a new state characterized by the emergence of a component of opposite helicity $-\sigma$ and change in the orbital angular momentum $l + 2\sigma$.

Let us consider the four redirected beams with wavevectors $\mathbf{k}_R = -\beta_0\hat{\boldsymbol{y}}, \mathbf{k}_L = +\beta_0\hat{\boldsymbol{y}}, \mathbf{k}_T = +\beta_0\hat{\boldsymbol{x}}, \mathbf{k}_B = -\beta_0\hat{\boldsymbol{x}}$ in our experimental case (Fig. 3a). These are produced by the PhCM at the BIC frequency. The overall effect of the BIC mode excitation, in a simplified model, is in that the incoming plane wave is abruptly redirected by the photonic structure in the momentum space along 4 specific directions dictated by the crystal symmetry. The fields of the redirected waves $\tilde{\boldsymbol{E}}_{\boldsymbol{o}}(\mathbf{k}_j)$, with $j = \{R, L, T, B\}$, combine themselves with the incident field over the PhC volume. We conjectured that the experimentally outcoupled waves of polarization $\tilde{\boldsymbol{E}}_w^{(j)}(\mathbf{k}_j)$ at angles $\theta_j = \theta_c = \frac{\pi}{2}$, with $\phi_j = (-\frac{\pi}{2}, \frac{\pi}{2}, 0, \pi)$, respectively, were proportional to the total field $\tilde{\boldsymbol{E}}_{\boldsymbol{o}}(\mathbf{k}_j) + \boldsymbol{E_i}$. The electric fields $\tilde{\boldsymbol{E}}_{\boldsymbol{o}}(\mathbf{k}_j)$ are obtained according to the geometric parallel transport transformation mediated by the operator $\hat{\mathcal{U}}(\theta_r, \phi)$. Finally, this reads

$$\tilde{\boldsymbol{E}}_w^{(j)}\left(\frac{\pi}{2}, \phi_j\right) \equiv (E^+_{w,j}, E^-_{w,j}, E^z_{w,j})^T \propto \left[\hat{\mathcal{U}}\left(\frac{\pi}{2}, \phi_j\right) + \hat{\mathcal{I}}\right]\boldsymbol{E_i}, \tag{S10}$$

where $\hat{\mathcal{I}} = \mathrm{diag}(1, 1, 1)$. This simple model does not take into account the spin-momentum locking associated with the inhomogeneous optical field characterized by transverse SAM density (Fig. 2, main paper). Compacting the variables of interest in the vector form $\boldsymbol{v_j} \equiv (\alpha, \beta, \phi_j)$, with $j \in \{R, L, T, B\}$, *i.e.* $\theta_r = \pi/2$ and $\phi_T = 0°, \phi_L = 90°, \phi_B = 180°$ and $\phi_R = 270°$ and considering the output field components $\{E^+_w(\boldsymbol{v_j}), E^-_w(\boldsymbol{v_j}), E^z_w(\boldsymbol{v_j})\}$, we can write

$$I(\boldsymbol{v_j}) = c_+|E^+_w(\boldsymbol{v_j})|^2 + c_-|E^-_w(\boldsymbol{v_j})|^2 + c_z|E^z_w(\boldsymbol{v_j})|^2, \tag{S11}$$

with $j \in \{R, L, T, B\}$, where the intensities of the outcoupled components are weighted with phenomenological coefficients $c_\pm$. Indeed, since the side waves possess a transverse SAM, which the direction of propagation is locked to, in the above expression we balanced the components with the coefficients $c_\pm$ admitting values in the range $(0, 1)$ to account for a possible *spin-polarized* coupling of input light to the mode. Experimentally, the intensities $I(\boldsymbol{v_j}) = I_j(\alpha, \beta)$ of the outcoupled waves were measured as a function of the input polarization $\boldsymbol{E_i}(\alpha, \beta)$ and fitted to the above equation. In particular, we fixed the HWP angle α to two values, $\alpha^S = 0$ (S-polarized input on the QWP) and $\alpha^P = \pi/4$ (P-polarized input on the QWP), and measured the intensities as a function of the QWP angle $\beta \in (0, 2\pi)$. This basic model allowed us to interpret all the experimental results reported in Fig, 4 and 5. It also predicted the experimental behavior actually observed upon rotation of the PhCM about the z axis with respect to the reference system. Indeed, the rotation of the crystal produced a variation of the geometric phase ϕ_j (for each redirected beam) with respect to the global reference system (input polarizer) as discussed in the main paper. The fitted chiral directivity

$$\eta = \frac{c_+ - c_-}{c_+ + c_-}, \tag{S12}$$

reached a value $\sim 99.9\%$ under optimal optical coupling, *i.e.* breaking the symmetry of the excitation at an angle of incidence $\theta_i = 0.03°$. In addition, opposite homologous waves, that is along $\mp\hat{\boldsymbol{y}}$ (R, L) and $\pm\hat{\boldsymbol{x}}$ (T, B), were characterized by opposite sign of η (see Tables 1,2 in Figs. 4,5).

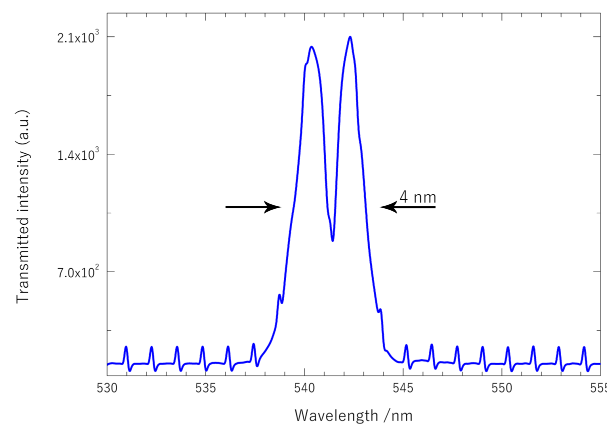

Fig. S4. Transmission spectrum through the PhCM excited with a single laser line centered at 541 nm. The supercontinuum laser was equipped with acousto-optic tunable filters allowing tunable filtering in the visible and near infrared. The power of each wavelength was controlled via software. The line bandwidth depends on the selected range. When the wavelength was set at 541 nm, a resonance peak appeared overlapped to the laser line (bandwidth 4 nm).

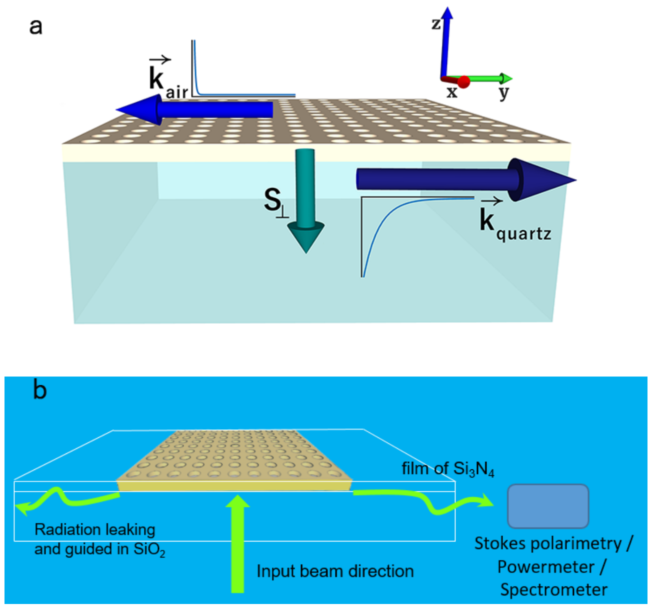

Fig. S5. Scheme. (a) Scheme of the side wave R having two evanescent components, *i.e.* at the interface with air (top) and quartz (bottom), both having a transverse SAM component along $\hat{z}$: only the bottom wave favorably propagates is SiO_2, as shown by the cartoon in **(b)** depicting the process of radiation leaks guided in SiO_2.

REFERENCES

1. G. Zito, G. Rusciano, and A. Sasso, "Dark spots along slowly scaling chains of plasmonic nanoparticles," Opt. Express **24**, 13584–13589 (2016).
2. G. Zito, G. Rusciano, and A. Sasso, "Enhancement factor statistics of surface enhanced raman scattering in multiscale heterostructures of nanoparticles," J. Chem. Phys. **145**, 054708 (2016).
3. K. Y. Bliokh and F. Nori, "Transverse and longitudinal angular momenta of light," Phys. Rep. **592**, 1–38 (2015).
4. A. Aiello, P. Banzer, M. Neugebauer, and G. Leuchs, "From transverse angular momentum to photonic wheels," Nat. Phot. **9**, 789–795 (2015).
5. Y. Yang, C. Peng, Y. Liang, Z. Li, and S. Noda, "Analytical perspective for bound states in the continuum in photonic crystal slabs," Phys. Rev. Lett. **113**, 037401 (2014).
6. K. Y. Bliokh, A. Y. Bekshaev, and F. Nori, "Extraordinary momentum and spin in evanescent waves," Nat. Commun. **5** (2014).
7. T. Van Mechelen and Z. Jacob, "Universal spin-momentum locking of evanescent waves," Optica. **3**, 118–126 (2016).
8. V. Mocella and S. Romano, "Giant field enhancement in photonic resonant lattices," Phys. Rev. B **92**, 155117 (2015).
9. R. Gansch, S. Kalchmair, P. Genevet, T. Zederbauer, H. Detz, A. M. Andrews, W. Schrenk, F. Capasso, M. Loncar, and G. Strasser, "Measurement of bound states in the continuum by a detector embedded in a photonic crystal," Light. Sci. & Appl. **5**, e16147 (2016).
10. C. W. Hsu, B. Zhen, J. Lee, S.-L. Chua, S. G. Johnson, J. D. Joannopoulos, and M. Soljačić, "Observation of trapped light within the radiation continuum," Nature. **499**, 188–191 (2013).
11. K. Y. Bliokh, E. A. Ostrovskaya, M. A. Alonso, O. G. Rodríguez-Herrera, D. Lara, and C. Dainty, "Spin-to-orbital angular momentum conversion in focusing, scattering, and imaging systems," Opt. Express **19**, 26132–26149 (2011).
12. K. Y. Bliokh, F. Rodríguez-Fortuño, F. Nori, and A. V. Zayats, "Spin-orbit interactions of light," Nat. Phot. **9**, 796–808 (2015).